

## Research

**Subject Areas:**

fluid mechanics, wave motion,  
geophysics

**Keywords:**

tsunami generation, gravity surface  
waves

**Author for correspondence:**

Leonardo Gordillo  
e-mail: leonardo.gordillo@univ-paris-  
diderot.fr

# Generation of surface waves by an underwater moving bottom: Experiments and application to tsunami modelling

---

Timothée Jamin<sup>1</sup>, Leonardo Gordillo<sup>1</sup>,  
Gerardo Ruiz-Chavarría<sup>2</sup>, Michael  
Berhanu<sup>1</sup>, Eric Falcon<sup>1</sup>

---

<sup>1</sup>Univ Paris Diderot, Sorbonne Paris Cité, MSC, UMR  
7057 CNRS, F-75013 Paris, France,

<sup>2</sup>Facultad de Ciencias, Universidad Nacional  
Autónoma de México, 04510 México D. F., México

We report laboratory experiments on surface waves generated in a uniform fluid layer whose bottom undergoes a sudden upward motion. Simultaneous measurements of the free-surface deformation and the fluid velocity field are focused on the role of the bottom kinematics in wave generation. We observe that the fluid layer transfers bottom motion to the free surface as a temporal high-pass filter coupled with a spatial low-pass filter. Both filter effects are usually neglected in tsunami warning systems. Our results display good agreement with a prevailing linear theory without fitting parameter. Based on our experimental data, we provide a new theoretical approach for the rapid kinematics limit that is applicable even for non-flat bottoms: a key step since most approaches assume a uniform depth. This approach can be easily appended to tsunami simulations under arbitrary topography.

## 1. Introduction

Most tsunamis are triggered by sudden displacements of the seabed during earthquakes. To predict tsunami hazards in real time, actual warning models require, first and foremost, data of the free-surface waveform in the open seas. Buoy networks dedicated to detect tsunamis may provide direct measurements of wave heights at fixed positions across the oceans [1]. When buoy records are unavailable, a faster indirect method based on fault and seismic data is used by default. The seabed displacement is computed numerically from the fault slip using Okada's model [2], and then transferred to the ocean free surface. Unfortunately, this technique often underestimates the surface wave amplitude (*e.g.* for the 2004 Sumatra-Andaman tsunami [3]).

Several reasons have been proposed to explain this bias [4–11], including the seabed-kinematics role during an earthquake (*i.e.* its spatiotemporal features) [11–14]. Bottom displacement is considered to be instantaneous if its typical rise time is small compared to the time scale of the generated waves at the free surface [13]. Most earthquakes meet this condition, although other remarkable tsunamigenic events barely satisfy it: for instance, in two of the hugest tsunami ever registered, the bottom displacements were noticeably slow [15]. Unfortunately, many numerical codes used in warning systems neglect seabed kinematics (*e.g.* the MOST [16] and the TUNAMI [17]). Instead, they use a transfer model that simply translates the source bottom final deformation to the ocean surface. Although available, numerical simulations that suitably do consider bed-sea kinematic coupling during displacements have high computation costs (*cf.* [18–21]) and require to know the bottom kinematics *a priori*. Strikingly, even if the deformation happens instantaneously, the free-surface displacement is not equal to the bottom one [22,23].

Laboratory experiments dealing with the influence of bed-uplift kinematics in tsunami generation are rare and have been based on measurements of the free-surface deformation [24,25], providing limited information about the fluid dynamics. Velocity measurements in the bulk are even rarer and only concern landslide-triggered tsunamis [26,27]. Furthermore, many laboratory experiments have been performed in channels and thus tend to overlook the three-dimensional (3D) geometry of real scenarios [25–28].

In this Letter, we analyse experimentally and theoretically the hydrodynamic coupling between the bottom and the free-surface motion in a 3D fluid layer, focusing on the role that the bottom kinematics plays in wave generation. For this purpose, we performed combined measurements of the free-surface deformation and the fluid velocity field. Our results are then compared with a linear theory [29]. We also provide a generalized framework that can be applied systematically to enhance tsunami warning-systems simulations.

## 2. Experimental Setup

We performed our experiments in a  $110 \times 110 \times 30 \text{ cm}^3$  Plexiglas basin filled with water to a depth of  $h = 2.5 \text{ cm}$ . A circular region (radius  $r_2 = 3.25 \text{ cm}$ ) was carved in the bottom centre and covered with a stretched elastic sheet. The sheet is deformed by means of a solid flat circular piston ( $r_1 = 2.5 \text{ cm}$ ) placed beneath the membrane and attached to an electromechanical shaker (see Fig. 1). As a result of the setup geometry, the bottom vertical motion can be described as a separable spatiotemporal function with circular symmetry,  $\zeta(r, t) = \zeta_m \alpha(r) \beta(t)$ , where  $\zeta_m$  is the maximal bottom deformation;  $\alpha(r)$  is the spatial profile along the radial horizontal coordinate  $r$  [see Fig. 1 (inset)] and  $\beta(t)$  is the displacement time function. The latter was arbitrary chosen to be an exponential rise,  $\beta_{\text{exp}}(t) = 1 - e^{-t/\tau_b}$ , or a half-sine one,  $\beta_{\text{sin}}(t) = \sin^2[\pi t / (2\tau_b)]$  if  $t \leq \tau_b$  or 1 if  $t > \tau_b$ ; where  $\tau_b$  is defined as the rise time. To achieve this, the shaker input signal was determined by exploiting the bottom velocity records from a laser Doppler vibrometer. Our system can be used to study rise times from 10 to 500 ms, and upward bottom amplitudes from 1.5 to 5 mm. Typical bottom velocities vary from 1 to  $30 \text{ cm} \cdot \text{s}^{-1}$ . The basin extent was chosen to avoid wave reflections on the lateral walls during the generation process.

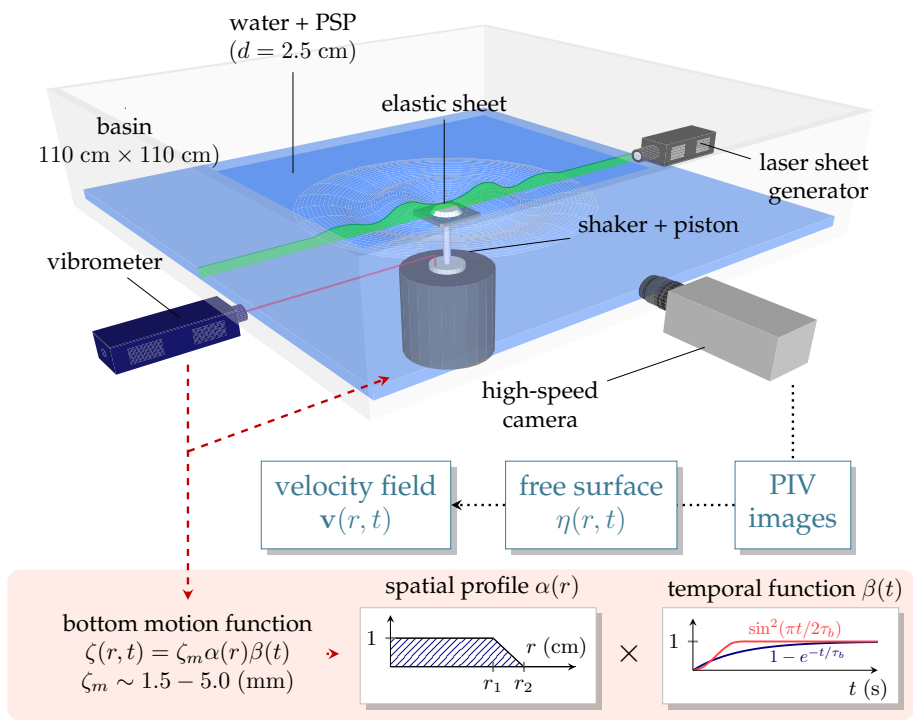


**Figure 1.** Main: Experimental setup. A layer of water is contained in a basin where a shaker and a piston vertically deform an elastic sheet placed at the bottom centre. The piston motion is recorded using a laser vibrometer. Images from a sectional cut of the fluid are obtained using a laser sheet generator and a high-speed camera. The bottom dimensionless spatial profile  $\alpha(r)$  and the time displacement function  $\beta(t)$  are also displayed.

The velocity field in the bulk during bottom and surface deformations is obtained using Particle Image Velocimetry (PIV). A laser sheet passing through the basin centre illuminated a vertical slice of water seeded with  $50\text{-}\mu\text{m}$  polyamide particles (see Fig. 1). This provided an imaging region of  $71 \times 30 \text{ mm}^2$  ( $1600 \times 692$  pixels) that was recorded at 500 Hz during 1 s. Since the system is axisymmetric, these measurements build a 3D picture of the flow. The surface of the water layer was blown with more particles to create an identifiable line on the images for detection. The free-surface vertical deformation  $\eta(r, t)$  was then obtained by applying a Radon transform algorithm on the images [30]. Finally, we applied a PIV grid-refining scheme [31] using an average correlation method [32] on ten experimental runs for each set of parameters. All the data used throughout this article is available at a public repository at [33].

The two time scales in our experiment are the bottom rise time  $\tau_b$  and the typical time of the generated waves  $\tau_w$ . We defined  $\tau_w$  as the semi-period of the wave, *i.e.* the time between the first maximum and minimum of the water surface deformation at the basin centre ( $r = 0$ ). In our experiment,  $\tau_w \simeq 130 \text{ ms}$  is the same for any displacement time function  $\beta$  and rise time  $\tau_b$  (see results below). This value is related to the dominant wavelength of the generated wave  $\lambda_w \simeq 10 \text{ cm}$  (according to acquired images), through the dispersion relation  $\tau_w = \pi / \sqrt{gk_w \tanh k_w h}$ . Accordingly, the experimental time ratio, defined as  $\bar{\tau} = \tau_b / \tau_w$  varies between 0.08 and 4. The relevance of the time ratio in tsunami generation was noticed by Hammack [25], who suitably identified three wave-response regimes to bottom deformations: impulsive ( $\bar{\tau} \ll 1$ ), transitional ( $\bar{\tau} \sim 1$ ), and creeping ones ( $\bar{\tau} \gg 1$ ).

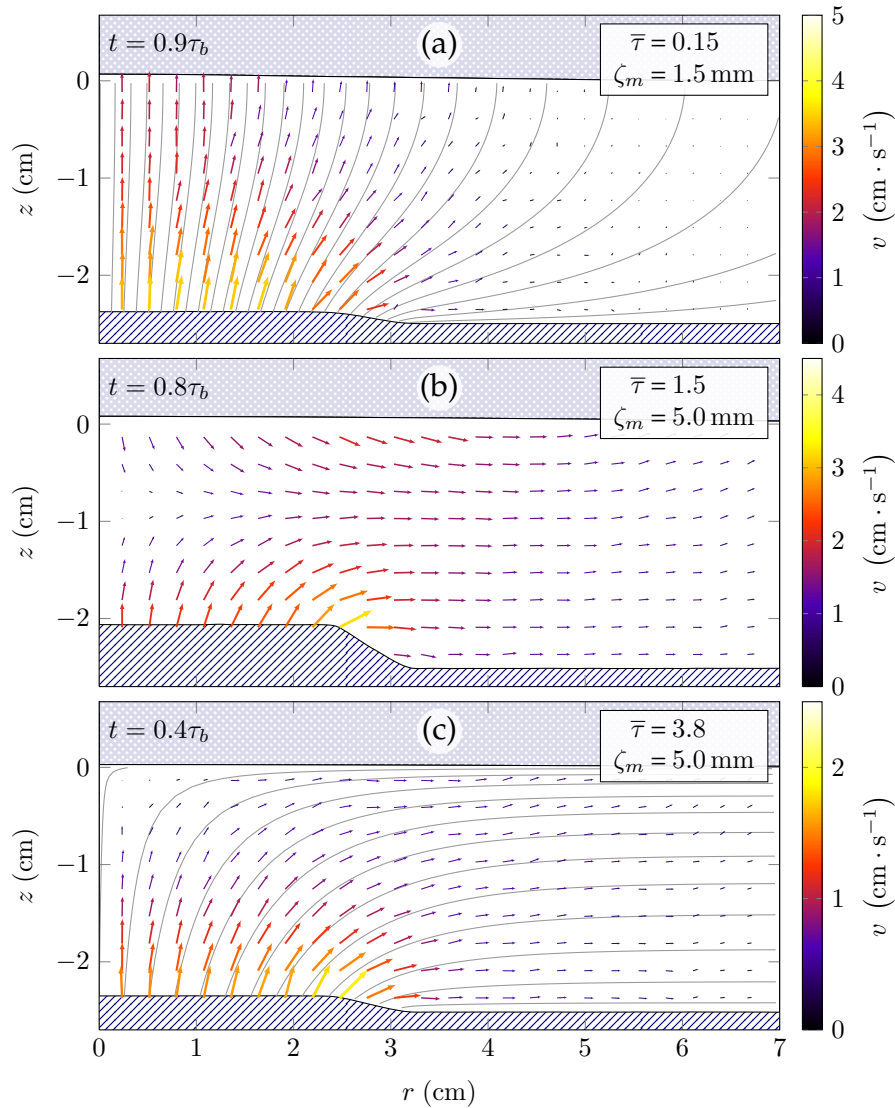


**Figure 2.** Experimental velocity fields in the water during half-sine bottom displacements for three typical  $\bar{\tau}$  values. The streamlines (set of grey curves) in (a) and (c) were computed numerically using an asymptotic model for the  $\bar{\tau} \ll 1$  and  $\bar{\tau} \gg 1$  cases (see explanation in text). In all cases, the free-surface deformation is significantly smoother than the bottom one.

### 3. Results and discussion

Within this classification, we display in Fig. 2 three characteristic snapshots of the generation velocity fields for half-sine type displacements. The vertical coordinate is denoted as  $z$  such that at rest, the free surface matches  $z = 0$ , and the bottom,  $z = -h$ . When  $\bar{\tau} \ll 1$ , we observe an upward global motion during the bottom uplift. Indeed, the velocity field just below the free surface is vertical [see Fig. 2(a)] as predicted in [34]. Gravity-wave propagation starts remarkably after the end of the bottom motion as shown in videos<sup>1</sup>. When  $\bar{\tau} \sim 1$ , the flow resembles that of Fig. 2(a) at short times. However, before the bottom motion ends, waves start to propagate radially from the generation region: an oscillating flow occurs right beneath the free surface [see Fig. 2(b)].

<sup>1</sup>See Supplemental Material at [URL] for velocity-field videos of the runs depicted in Fig. 2.

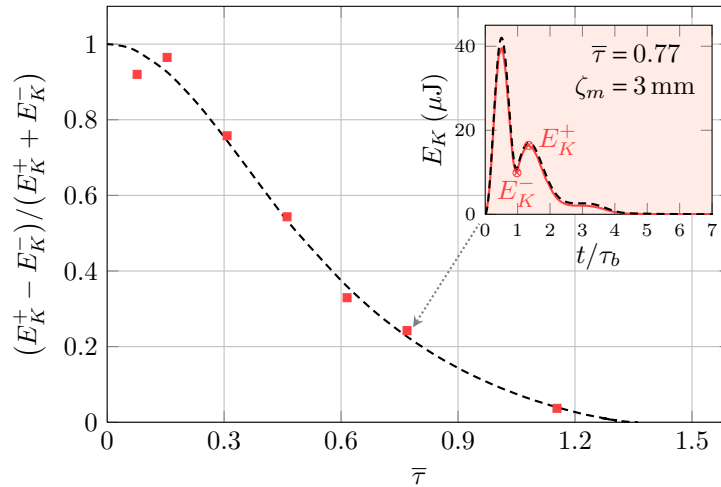


**Figure 3.** Inset: Experimental (solid line) and theoretical (dashed line) kinetic energy  $E_K$  versus time.  $E_K^-$  is the local minimum of kinetic energy near  $t = \tau_b$  and  $E_K^+$  is the local maximum of kinetic energy due to the wave propagation. Main: Experimental (squares) and theoretical (dashed line) contrast of kinetic energy versus  $\bar{\tau}$ .

In this case, both bottom deformation and wave propagation occur simultaneously suggesting that the bottom kinematics affects induced waves. For  $\bar{\tau} \gg 1$ , the free surface remains mostly stationary and accordingly, the vertical component of the velocity vanishes when approaching the free surface [see Fig. 2(c)]. In this stage, the outward flow reminds that of a moving bottom in presence of a fixed boundary at  $z = 0$ .

To quantify the transition between the slow and rapid regimes, we compute the kinetic energy from the fluid velocity field. Figure 2 shows that the region  $r < 7$  cm contains most of the kinetic energy during the bottom deformation. As shown in Fig. 3 (inset), the kinetic energy within this volume,  $E_K$ , captures also the main temporal features of the motion (see also [35]). The bottom uplift induces an intense first maximum of  $E_K$ . As the bottom stops afterwards, a local minimum  $E_K^-$  appears and later, a second maximum  $E_K^+$  emerges induced by wave propagation. We define the contrast of kinetic energy as  $(E_K^+ - E_K^-) / (E_K^+ + E_K^-)$ . As shown in Fig. 3, the contrast is close to unity for  $\bar{\tau} \ll 1$ : the liquid can be considered as motionless at the end of the bottom deformation ( $E_K^- \approx 0$ ), with its velocity being negligible compared to those due to wave propagation. Inertia seems to be absent since no flow outlasts the bottom motion: the liquid layer and the bottom behaves like a single block. For larger  $\bar{\tau}$ , the wave propagation begins while the bottom is still moving so the energy contrast decreases to zero. Furthermore, for  $\bar{\tau} \gtrsim 1.4$ , the contrast is not any more defined because the bottom deformation and the wave propagation overlap so much that  $E_K^-$  and  $E_K^+$  do not exist at all. This shows that the energy contrast depicts well the transition between rapid and slow scenarios.

Since the fluid velocity field is coupled with the free-surface deformation, both quantities share similar spatiotemporal features. In Fig. 4, we depict the bottom and the free-surface elevations at  $r = 0$ ,  $\zeta_0$  and  $\eta_0$ , as a function of time. We observe in all cases that the free surface and the bottom are synchronized at the beginning of the motion. For  $\bar{\tau} \ll 1$  this is true throughout the bottom uplift and regardless of the displacement time function  $\beta(t)$  as time satisfies  $t < \tau_b \ll \tau_w$  [see Figs. 4(a)-4(b)]. Besides, the subsequent stage is independent of the displacement-time history of the bottom. Contrariwise, for  $\bar{\tau} \gtrsim 1$ , exponential and half-sine bed displacements induce free-surface responses that not only differ from rapid ones, but also from one another [see Figs. 4(c)-4(d)], *e.g.* the negative part of  $\eta_0$  is more pronounced for the half-sine case. This evidences that for

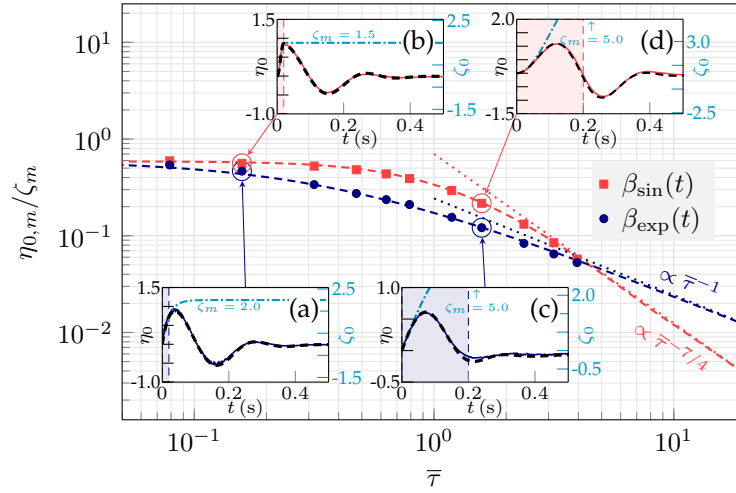


**Figure 4.** Insets: Bottom and free-surface deformations in mm at  $r = 0$ ,  $\zeta_0$  and  $\eta_0$ , versus time ( $\zeta_0$  in dash-dotted lines;  $\eta_0$  experiments in solid, theory in dashed lines) for exponential (a and c) and half-sine (b and d) bottom displacements. The vertical dashed lines represent  $t = \tau_b$  for each run. The wave time scale  $\tau_w$  is found to be 130 ms in all the cases. Main: Dimensionless free-surface maximal elevation at  $r = 0$ , against  $\bar{\tau}$  for different bottom displacements (see legend). Symbols are experimental data, dashed lines are theoretical results and dotted lines are asymptotic behaviours ( $\bar{\tau} \gg 1$ ).

$\bar{\tau} \gtrsim 1$  the generated-wave shape depends on the nature of  $\beta(t)$  as well as on its typical time  $\tau_b$ , which confirms that the bottom kinematics is crucial in non-impulsive wave generation.

To understand more precisely its role, we plot in Fig. 4 (main) the dimensionless maximal elevation of the free surface at  $r = 0$ ,  $\eta_{0,m}/\zeta_m$ , as a function of the time ratio  $\bar{\tau}$ . As expected,  $\eta_{0,m}$  decreases with  $\bar{\tau}$  and converges to the same asymptote for  $\bar{\tau} \ll 1$  independently of the nature of  $\beta(t)$ . For  $\bar{\tau} \gg 1$ , we observe two different behaviours:  $\eta_{0,m}$  decreases as  $\tau_b^{-1}$  for exponential bottom displacements and as  $\tau_b^{-7/4}$  for half-sine ones. This differs from 1D experiments where a  $\tau_b^{-1}$  power law fits both cases [25]. To summarize, when motion is transferred from the bottom to the free surface, the fluid layer behaves as a temporal high-pass filter (cut-off at  $\bar{\tau}^{-1} \approx 1$ ).

The experimental data displayed in Figs. 3-4 as well as the spatial profiles (not shown herein), are all found to be in good agreement with theoretical curves without fitting parameters. These were calculated using the axisymmetric version of Hammack's tsunami-generation theory [29] Capillary and viscosity effects can be neglected since  $\lambda_w \gg 2\pi\sqrt{\gamma/(\rho g)}$  ( $\gamma$  is the surface tension and  $\rho$  the fluid density) and  $r_1 \gg \sqrt{\nu\tau_b}$  ( $\nu$  is the kinematic viscosity). The flow is assumed to be irrotational and incompressible ( $c_s\tau_b \gg \{\zeta_m, h, r_1\}$  where  $c_s$  is the sound speed in water [36]). Hence the system can be expressed in terms of a velocity potential  $\phi$  that satisfies

$$\nabla^2 \phi = 0 \quad (3.1)$$

in the bulk. The experimental amplitude parameter  $\zeta_m/h$  is small enough to linearize boundary conditions [29]. Thus, if the bottom is initially flat, the dynamic condition at the free surface as well as the kinematic boundary conditions can be written as

$$\partial_t \phi|_{z=0} + g\eta = 0. \quad (3.2)$$

$$\partial_z \phi|_{z=-h} - \partial_t \zeta = 0, \quad (3.3)$$

$$\partial_z \phi|_{z=0} - \partial_t \eta = 0. \quad (3.4)$$

To solve this system of equations, we apply the Laplace transform in  $t$  to the displacement time function,  $\tilde{\beta}(s) \equiv \mathcal{L}\{\beta(t)\}(s)$ , and the Hankel transform of zeroth order in  $r$  to the spatial profile,

$\hat{\alpha}(k) \equiv \mathcal{H}_0\{\alpha(r)\}(k) \equiv \int_0^{+\infty} \rho J_0(kr) \alpha(r) dr$ , where  $J_0$  is the zeroth order Bessel function of the first kind. The latter is equivalent to a two-dimensional (2D) Fourier transform under circular symmetry. Accordingly, the Hankel transform of the free-surface deformation may be written as [29]

$$\hat{\eta}(k, t) = \frac{\zeta_m \hat{\alpha}(k)}{\cosh kh} \cdot \mathcal{L}^{-1} \left\{ \frac{s^2 \tilde{\beta}(s)}{s^2 + \omega(k)^2} \right\} (k, t). \quad (3.5)$$

where  $\omega(k) = \sqrt{gk \tanh kh}$  is the gravity-wave dispersion relation. The direct and inverse Laplace transforms in Eq. (3.5) can be evaluated in closed form for both  $\beta_{\text{exp}}(t)$  and  $\beta_{\text{sin}}(t)$ . Besides, the spatial transform  $\hat{\alpha}(k)$  may be computed numerically. The spatiotemporal free-surface deformation  $\eta(r, t) = \mathcal{H}_0^{-1}\{\hat{\eta}(k, t)\}$  can be found likewise using a Fourier-Bessel series representation of  $\mathcal{H}_0^{-1}$  [37]. The velocity field can also be obtained by calculating the velocity potential  $\phi$  through analogous formulas.

Remarkably, the first factor in Eq. (3.5) is the Hankel transform of the final bottom deformation but modulated with a low-pass filter,  $(\cosh kh)^{-1}$ , that smooths the free surface (see Fig. 2). The second factor is spatiotemporal and relates the time  $t$  (corresponding to  $s$  in the Laplace domain) with the two characteristic times: the wave semi-period  $\tau_w$  (corresponding to  $\omega$ ) and the bottom rise time  $\tau_b$  (contained in  $\tilde{\beta}(s)$ ). When  $t \ll \tau_w$ ,  $s^2 + \omega^2 \sim s^2$ , the second factor of Eq. (3.5) becomes simply  $\beta(t)$ , gravity effects vanish yielding interface elevations instantaneously equal to the bottom low-pass-filtered deformations. This is consistent with the behaviour observed at short times in Fig. 4 (insets), where the free surface moves synchronously with the bottom. When  $t \gtrsim \tau_b$ ,  $\beta(t)$  can be considered as a Heaviside function if  $\bar{\tau} \ll 1$ . Hence,  $\tilde{H}(s) = s^{-1}$ , and the second factor in Eq. (3.5) becomes a propagation term  $\cos[\omega(k)t]$ . As stated by Kajiura [22], this is equivalent to a Cauchy-Poisson wave problem in which only the final bottom deformation is low-pass filtered and translated to the surface as an initial condition. Likewise, we have shown that the fluid is motionless when the bottom motion ends. No trace from the initial motion is left. This explains the memory loss of the bottom-displacement history observed in our experiments.

The impulsive limit ( $\bar{\tau} \ll 1$ ) has a striking feature: gravity plays no role during the bottom motion ( $t < \tau_b$ ). Accordingly, we can drop the gravity term in Eq. (3.2), so  $\phi|_{z=0} = 0$  and the free surface  $\eta$  decouples from Eqs. (3.1-3.3). This yields a decoupled boundary value problem (DBVP) for the velocity potential  $\phi$ . In Fig. 2(a), we depict the streamlines obtained from solving numerically the DBVP. This numerical method differs from the Green function approach developed in [34]. The streamlines are steady for  $t < \tau_b$ . Likewise, another DBVP can be found for the  $\bar{\tau} \gg 1$  case:  $g \rightarrow \infty$ , hence  $\partial_z \phi|_{z=0} = 0$ , which yields the streamlines of Fig. 2(c). For both limits,  $\bar{\tau} \gg 1$  and  $\bar{\tau} \ll 1$ , the computed streamlines fit very well the experimental velocity field [see Figs. 2(a) and 2(c)]. While for  $\bar{\tau} \gg 1$ ,  $\eta \simeq 0$ , for initially flat bottoms undergoing impulsive uplifts ( $\bar{\tau} \ll 1$ ),  $\eta$  can be obtained from Eq. (3.4). This leads to the spatial low-pass filtered results found previously. The DBVP approach has a great advantage: it can be adapted to arbitrary-bottom-shaped basins by simply writing the bottom condition as  $\partial_z \phi|_{z=-h(x,y)} = \partial_t \zeta$ . We strongly recommend this method as a computationally affordable routine in actual simulations for incorporating terrain conditions during tsunami generation. To compare our results ( $\dagger$ ) with real tsunami scenarios ( $*$ ), consider two dimensionless parameters: the time ratio  $\bar{\tau}$  and the size scale  $r_1/h$ . For tsunamis ( $\zeta_m^*, h^*, r_1^*$ )  $\sim$  (10 m, 5 km, 80 km) and  $\tau_b^* \in [1, 100]$  s [13,25]. Notice that for tsunamis and our experiments,  $\zeta_m/h \ll 1$ , so the linear theory is valid,  $\eta \propto \zeta_m$  and  $\zeta_m$  can be rescaled out from Eq. (3.5). Concerning  $\bar{\tau}$ , the tsunami range  $\bar{\tau}^* \in [0.003, 0.3]$  is located on the left-hand side of Fig. 4 since here  $\bar{\tau}^\dagger \in [0.08, 4]$ . The temporal high-pass filter becomes significant for slowest scenarios ( $\eta_{0,m}^*/\zeta_m^*$ -corrections from 10% to 40% for  $\bar{\tau}^* \sim 0.3$ ). Although fastest tsunamis are beyond our experimental range, the asymptote for  $\bar{\tau} \ll 1$  is largely attained within it. Concerning the other parameter, we fixed  $r_1^\dagger/h^\dagger = 1$  to highlight the spatial low-pass filtering. For accepted tsunami values ( $r_1^*/h^* \sim 16$ ) these filtering effects are expected to be weak. However, recent and more direct evidence shows that tsunami initial waveforms have a complex spatial distribution with significantly smaller length scales:  $r_1^*/h^* \lesssim 5$  [38,39]. For a spherical-cap deformation, this yields low-pass filtering  $\eta_{0,m}^*/\zeta_m^*$ -corrections of 10% [22]. Besides, ocean depth

near subduction tsunamigenic regions varies abruptly, *e.g.* 80% along 50 km in the fault crosswise direction. Such terrain geometry provides further significant corrections [34]. It is at this point where a general-bathymetry DBVP approach will become useful.

## 4. Conclusions

In conclusion, we have investigated the generation of surface waves by an underwater moving bottom. The experiments, which included simultaneous measurements of fluid velocity field and free-surface displacement in an initial flat bottom configuration, display excellent agreement without fitting parameter with a linear theory of gravity waves. Essentially, the fluid layer transfers motion from the bottom to the free surface as a temporal high-pass filter coupled with a spatial low-pass filter. Transfer models that perform a simple translation as those used by tsunami warning systems, overlook both filters effects. Supported on measured velocity fields, we have developed an alternative guideline for taking into account spatial filtering in impulsive bottom uplifts. Furthermore, we can use our model to include in situ bathymetry data at low computational cost: a key for improving tsunami simulations in real scenarios.

## Acknowledgement

We thank A. Lantheaume and the LIED for their technical help. T. J. was supported by the DGA-CNRS Ph.D program and L. G., by a 2012 Postdoctoral Fellowship of the AXA Research Fund. G. R. was supported by the program Research in Paris 2011 of the City of Paris. This research was financed by the ANR Turbulon 12-BS04-0005.

## References

1. Mungov, G., Eblé, M. & Bouchard, R., 2012 DART® Tsunameter Retrospective and Real-Time Data: A Reflection on 10 Years of Processing in Support of Tsunami Research and Operations. *Pure Appl. Geophys.* p. 42. (doi:10.1007/s00024-012-0477-5).
2. Okada, Y., 1985 Surface deformation due to shear and tensile faults in a half-space. *Bull. Seismol. Soc. Am.* **75**, 1135–1154.
3. Geist, E. L., Titov, V. V. & Synolakis, C., 2006 Tsunami: WAVE of CHANGE. *Sci. Am.* **294**, 56–63. (doi:10.1038/scientificamerican0106-56).
4. Geist, E. L., Bilek, S. L., Arcas, D. & Titov, V. V., 2006 Differences in tsunami generation between the December 26, 2004 and March 28, 2005 Sumatra earthquakes. *Earth Planets Space* **58**, 185–193.
5. Maeda, T., Furumura, T., Sakai, S. & Shinohara, M., 2011 Significant tsunami observed at ocean-bottom pressure gauges during the 2011 off the Pacific coast of Tohoku Earthquake. *Earth Planets Space* **63**, 803–808. (doi:10.5047/eps.2011.06.005).
6. Tanioka, Y. & Seno, T., 2001 Sediment Effect on Tsunami Generation of the 1896 Sanriku Tsunami Earthquake. *Geophys. Res. Lett.* **28**, 3389–3392.
7. Dutykh, D. & Dias, F., 2010 Influence of sedimentary layering on tsunami generation. *Comput. Methods Appl. Mech. Engrg.* **199**, 1268–1275. (doi:10.1016/j.cma.2009.07.011).
8. Synolakis, C., Bardet, J. P., Borrero, J. C., Davies, H. L., Okal, E. A., Silver, E. A., Sweet, S. & Tappin, D. R., 2002 The slump origin of the 1998 Papua New Guinea Tsunami. *Proc. Roy. Soc. Lond. A* **458**, 763–789. (doi:10.1098/rspa.2001.0915).
9. Okal, E. A. & Synolakis, C., 2004 Source discriminants for near-field tsunamis. *Geophys. J. Int.* **158**, 899–912. (doi:10.1111/j.1365-246X.2004.02347.x).
10. Sammarco, P. & Renzi, E., 2008 Landslide tsunamis propagating along a plane beach. *J. Fluids Mech.* **598**, 107–119. (doi:10.1017/S0022112007009731).
11. Geist, E. L., Titov, V. V., Arcas, D., Pollitz, F. F. & Bilek, S. L., 2007 Implications of the 26 December 2004 Sumatra-Andaman Earthquake on Tsunami Forecast and Assessment Models for Great Subduction-Zone Earthquakes. *Bull. Seismol. Soc. Am.* **97**, S249–S270. (doi:10.1785/0120050619).
12. Synolakis, C., Liu, P., Carrier, G. & Yeh, H., 1997 Tsunamigenic Sea-Floor Deformations. *Science* **278**, 598. (doi:10.1126/science.278.5338.598).



13. Geist, E. L., 1998 Local tsunamis and earthquake source parameters. *Adv. Geophys.* **39**, 117–209.
14. Todorovska, M. I. & Trifunac, M. D., 2001 Generation of tsunamis by a slowly spreading uplift of the sea floor. *Soil. Dyn. Earthq. Eng.* **21**, 151–167. (doi:10.1016/S0267-7261(00)00096-8).
15. Kanamori, H., 1972 Mechanism of tsunami earthquakes. *Phys. Earth Planet In.* **6**, 346–359. (doi: 10.1016/0031-9201(72)90058-1).
16. Titov, V. V. & Gonzalez, F. I., 1997 Implementation and testing of the method of splitting tsunami (MOST) model. Technical Report NOAA Technical Memorandum ERL PMEL-112, Seattle.
17. UNESCO, 1997 IUGG/IOC Time Project: Numerical method of tsunami simulation with the leap-frog scheme. Technical Report IOC Manuals and Guides No. 35, Paris.
18. Ichiye, T., 1958 A theory on the generation of tsunamis by an impulse at the sea bottom. *J. Oceanogr. Soc. Japan* **14**.
19. Aida, I., 1969 Numerical experiments for tsunamis caused by moving deformations of the sea bottom. *B. Earthq. Res. I. Tokyo* **47**, 849–862. ISSN 0040-8972.
20. Kervella, Y., Dutykh, D. & Dias, F., 2007 Comparison between three-dimensional linear and nonlinear tsunami generation models. *Theor. Comput. Fluid Dyn.* **21**, 245–269. (doi:10.1007/s00162-007-0047-0).
21. Kakinuma, T., 2009 Numerical simulation of tsunami generation. In *Mathematical Physics and Application of Nonlinear Wave Phenomena*, pp. 14–21.
22. Kajiura, K., 1963 The leading wave of a tsunami. *B. Earthq. Res. I. Tokyo* **41**, 535–571. ISSN 0040-8972.
23. Dutykh, D., Dias, F. & Kervella, Y., 2006 Linear theory of wave generation by a moving bottom. *Cr. Acad. Sci. I - Math.* **343**, 499–504. (doi:10.1016/j.crma.2006.09.016).
24. Takahasi, R. & Hatori, T., 1962 A model experiment on the Tsunami generation from a bottom deformation area of elliptic shape. *B. Earthq. Res. I. Tokyo* **40**, 873–883.
25. Hammack, J. L., 1973 A note on tsunamis: their generation and propagation in an ocean of uniform depth. *J. Fluids Mech.* **60**, 769–799. (doi:10.1017/S0022112073000479).
26. Fritz, H. M., Hager, W. H. & Minor, H. E., 2003 Landslide generated impulse waves. 1. Instantaneous flow fields. *Exp. Fluids* **35**, 505–519. (doi:10.1007/s00348-003-0659-0).
27. Fritz, H. M., Hager, W. H. & Minor, H. E., 2003 Landslide generated impulse waves. 2. Hydrodynamic impact craters. *Exp. Fluids* **35**, 520–532. (doi:10.1007/s00348-003-0660-7).
28. Viroulet, S., Sauret, A. & Kimmoun, O., 2014 Tsunami generated by a granular collapse down a rough inclined plane. *Europhys. Lett.* **105**, 34004. (doi:10.1209/0295-5075/105/34004).
29. Hammack, J. L., 1972 *Tsunamis - A model of their generation and propagation*. Ph.D. thesis, California Institute of Technology - W. M. Keck Laboratory of Hydraulics and Water Resources, Pasadena, CA.
30. Sanchis, A. & Jensen, A., 2011 Dynamic masking of PIV images using the Radon transform in free surface flows. *Exp. Fluids* **51**, 871–880. (doi:10.1007/s00348-011-1101-7).
31. Westerweel, J., Dabiri, D. & Gharib, M., 1997 The effect of a discrete window offset on the accuracy of cross-correlation analysis of digital PIV recordings. *Exp. Fluids* **23**, 20–28. (doi:10.1007/s003480050082).
32. Meinhart, C. D., Wereley, S. & Santiago, J., 2000 A PIV algorithm for estimating time-averaged velocity fields. *J. Fluids Eng.* **122**, 285–289.
33. Gordillo, L., Jamin, T., Ruiz-Chavarría, G., Berhanu, M. & Falcon, E. Experiments on tsunami waves. *figshare*. (doi:10.6084/m9.figshare.979238).
34. Tyvand, P. A. & Storhaug, A. R. F., 2000 Green functions for impulsive free-surface flows due to bottom deflections in two-dimensional topographies. *Phys. Fluids* **12**, 2819–2833. (doi:10.1063/1.1290392).
35. Dutykh, D. & Dias, F., 2009 Energy of tsunami waves generated by bottom motion. *Proc. Roy. Soc. Lond. A* **465**, 725–744. (doi:10.1098/rspa.2008.0332).
36. Nosov, M. A., 1999 Tsunami generation in compressible ocean. *Physics and Chemistry of the Earth Part B* **24**, 437–441. (doi:10.1016/S1464-1909(99)00025-8).
37. Arfken, G.B. & Weber, H.J., 2005 *Mathematical Methods for Physicists*. Oxford, UK: Elsevier Academic Press, 6th edition.
38. Fujii, Y. & Satake, K., 2008 Tsunami waveform inversion of the 2007 Bengkulu, southern Sumatra, earthquake. *Earth Planets Space* **60**, 993–998.
39. Fujii, Y., Satake, K., Sakai, S., Shinohara, M. & Kanazawa, T., 2011 Tsunami source of the 2011 off the Pacific coast of Tohoku Earthquake. *Earth Planets Space* **63**, 815–820. (doi:10.5047/eps.2011.06.010).